

# Computational Investigation of Nonideal Higher Ionization Carbon Plasma Under Simulated High Heat Fluxes in Fusion Tokamak Reactors

N. M. E. Khalafallah<sup>1</sup> · S. Y. El-Bakry<sup>1</sup> · B. F. Mohamed<sup>2</sup> · M. A. Bourham<sup>3</sup>

Published online: 9 April 2017  
© Springer Science+Business Media New York 2017

**Abstract** Plasma-facing materials in future large tokamaks will suffer from ablation due to expected hard disruptions, which affects the reactor interior lining tiles and the divertor modules. Ablation and surface evaporation due to the intense heat flux from disruption is associated with ionization of the evolved particulates. Generated ions at such plasma conditions may allow for higher ionization states such that the plasma at the boundary can be composed of electrons, ions (first, second and third ionization) and excited atoms. The boundary layer is dense and tends to be weakly nonideal. The NC State University electrothermal plasma code ETFLOW used to simulate the high heat flux conditions in which the carbon liner tested for simulated heat fluxes for transient discharge period of 100  $\mu\text{s}$ , with FWHM of  $\sim 50 \mu\text{s}$ , to provide a wide range for obtaining reasonable good fits for the scaling laws. Transient events with  $\sim 10 \text{ MJ/m}^2$  energy deposition over short transient of 50–100  $\mu\text{s}$  would produce heat fluxes of 100–200  $\text{GW/m}^2$ . The heat flux range in this simulation is

up to 288  $\text{GW/m}^2$  to explore the generation of carbon plasma up to the third ionization  $\text{C}^{+++}$ . The generation of such heat fluxes in the electrothermal plasma source requires discharge currents of up to 250 kA over a 100  $\mu\text{s}$  pulse length with  $\sim 50 \mu\text{s}$  FWHM. The number density of the third ionization is six orders of magnitude less than the first ionization at the lowest heat flux and two orders of magnitude less at the highest heat flux. Plasma temperature varies from 31,600 K (2.722 eV) to 47,500 K (4.092 eV) at the lowest and highest heat fluxes, respectively. The plasma temperature and number density indicate typical high-density weakly nonideal plasma. The evolution of such high-density plasma particles into the reactor vacuum chamber will spread into the vessel and nucleate on the other interior components. The lifetime of the PFCs will shorten if the number of hard disruptions at such extreme heat fluxes would be increasing, resulting in major deterioration of the armor tiles.

**Keywords** Plasma facing materials · Tokamak hard disruptions · High heat flux ablation · High ionization carbon ions · High-density nonideal plasma

✉ M. A. Bourham  
bourham@ncsu.edu

N. M. E. Khalafallah  
nmkhalaf@ncsu.edu

S. Y. El-Bakry  
elbakry\_salah@yahoo.com

B. F. Mohamed  
mohamedbahf@yahoo.co.uk

<sup>1</sup> Physics Department, Faculty of Science, Ain-Shams University, Cairo, Egypt

<sup>2</sup> Plasma Physics Department, Nuclear Research Centre, Atomic Energy Authority, Cairo, Egypt

<sup>3</sup> Department of Nuclear Engineering, North Carolina State University, Raleigh, NC 27695, USA

## Introduction

Plasma-facing components (PFC) in future fusion reactors can suffer from intense high heat flux deposition and particle impacts during a plasma disruption, which affects the PFC causing ablation/vaporization resulting in a removal of thin layers from the surface. It may also cause structural damage by inducing crack formation and propagation, deterioration of the material, and mixed melting/vaporization for metallic components [1–3]. Graphite and carbon-fiber-composites proposed as interior reactor first wall tiles,

and some studies proposed using graphite as the top layer on the divertor modules [4–8]. Expected frequent disruptions and loss of plasma confinement will greatly affect the performance of the PFC materials and may require frequent replacements of the armor tiles.

Disruption-like events could be simulated experimentally and computationally using electrothermal plasma sources in capillary geometry, and have shown to be an effective technique to study erosion of plasma facing components (PFC) exposed to intense transient heat fluxes. Typical electrothermal plasma sources used for such studies are capillaries with an inner radius of 2–3 mm and 9–10 cm in length, which can generate weakly, nonideal, very dense, ( $10^{22}$ – $10^{28}/\text{m}^3$ ) and hot plasmas (1–5 eV) suitable for simulation of the expected disruptions in future fusion reactors [9–11]. It is of importance to investigate and be able to predict, the materials response to high-heat fluxes for radiant heat transport in tokamak fusion reactors, which causes surface ablation, melting, degradation, cracking, and generation of particulates that transport into the reactor vacuum vessel. Such generated particulates can be in micro or nano sizes, spreading into the reactor chamber, agglomerate and redeposited on the interior components [12, 13]. Energy deposition in the range of  $10 \text{ MJ}/\text{m}^2$  over a short transient of 50–100  $\mu\text{s}$  would produce heat fluxes of up to  $200 \text{ GW}/\text{m}^2$  (upper range for 50  $\mu\text{s}$ ) or  $100 \text{ GW}/\text{m}^2$  (lower range for 100  $\mu\text{s}$ ). During such undesirable events, the ablated material due to evaporation will dissociate, ionize then recombine after the cease of the disruption event. Interior plasma-facing materials (PFM), such as the divertor and first wall tiles, may suffer surface damage due to such disruption event with heat fluxes up to  $100 \text{ GW}/\text{m}^2$  or higher [13–15]. Carbon tiles (graphite and CFC) are low- $z$  materials considered as lining materials in the interior of the reactor chamber, as well as the divertor modules [4–8, 16–18]. In this research, selection of carbon is an example of a test material, possible tiles in fusion reactors, to experience generation of higher ionizations due to high-heat flux deposition that causes ablation followed by ionization.

Upon high-heat flux deposition on PFC surface, the ablated particulates will ionize at least at the singly ionized state, but not all ablated particulates will necessarily fully ionize. However, higher ionizations may take place to the second and third ionization states for a fraction of the total ablated mass. Carbon ablation from the PFC due to high-heat flux deposition may undergo higher ionization to  $\text{C}^+$ ,  $\text{C}^{++}$  and  $\text{C}^{+++}$  thus forming highly ionized carbon ions spreading in the reactor vacuum vessel and deposit their energy on the interior vessel components.

Carbon ablation at due to high-heat flux deposition can be simulated using electrothermal (ET) plasma capillary sources, which are good devices to simulate disruption-like

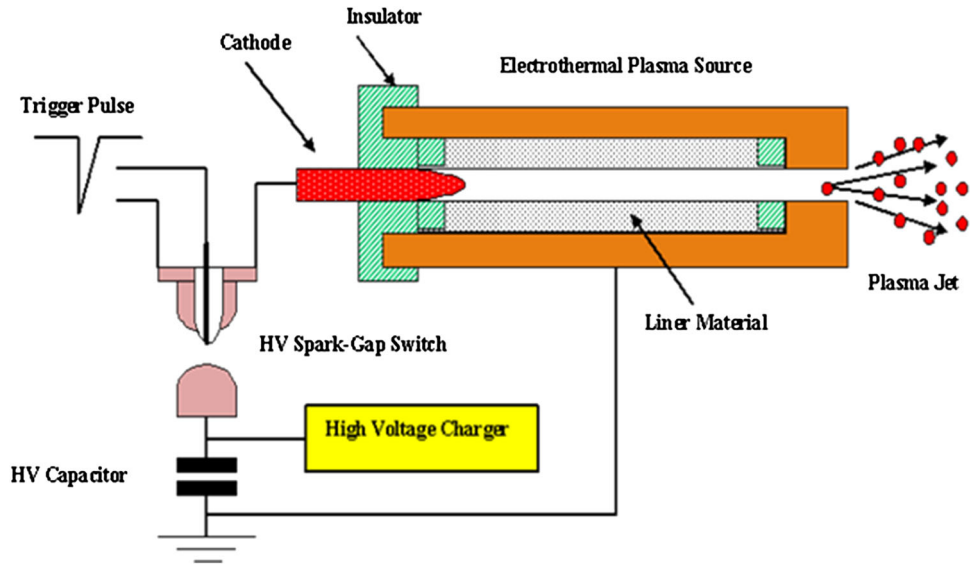
conditions [9–12]. Several experiments using ET sources in a short transient pulsed mode, as well as electron beam experiments have been used to evaluate surface erosion of PFCs under conditions typical to those expected in future fusion large tokamak devices [9, 10, 19, 20]. Several researchers using different computational modeling and techniques to evaluate PFC surface erosion and melting [11, 14, 15, 21, 22]. In most research, the focus on PFCs is on their erosion or melting (for metallic components) and the composition of the eroded ionized species. For carbon material tiles, the erosion may result in the ejection of carbon atoms, and carbon ions. The higher ionization of carbon ions may result from intense high heat flux. It is important to investigate how higher ionizations of carbon atoms may be achieved in a disruption-like event and what is the threshold of high heat flux that would allow the generation of higher ionizations to the second ( $\text{C}^{++}$ ) and third ( $\text{C}^{+++}$ ) ionized carbon ions. The study focuses on carbon as a low- $Z$  material and as a potential candidate in tiling critical components and first wall in future fusion reactors, as well as its ability to withstand disruptions with low ablation rates and is extensively used for plasma-facing components in present-day experimental fusion devices [3, 5–8, 23].

### Electrothermal Capillary Plasma Source

Electrothermal (ET) plasma capillary sources are good simulators for generating high-heat flux conditions expected in tokamak disruptions. Several ET sources were experimented to evaluate the erosion of several materials including fusion-relevant ones [9–12]. Additional applications of ET sources are their utilization as mass accelerator for fusion fueling to inject frozen fusion pellets at high speeds into the core of fusion reactors [24]. It is also a useful tool to investigate the electrical conductivity of ET plasmas within ideal and nonideal regimes [25].

Among the various codes written for simulation of ET capillary sources is the ETFLOW “ElectroThermal FLOW”, and has shown to be adequate to simulate disruption-like condition and calculates the erosion of materials under such high-heat flux deposition, details of the ETFLOW code are available elsewhere [24–28]. Figure 1 illustrates a pictorial of the basic parts of an electrothermal plasma source, which is a capillary discharge operating in the ablation-controlled arc regime [24, 25]. Generally, the generated plasma is of high density (up to  $10^{28}/\text{m}^3$ ) and low-to-moderate kinetic plasma temperature (1–5 eV), at high pressure (up to several thousand MPa), making such plasma nearly nonideal [26, 27]. The code includes a nonideal model for the energy-averaged electron–ion momentum transport cross-section, which affects the

**Fig. 1** Electrothermal plasma source showing basic components [24, 25]



plasma conductivity and the joule heating in the energy equation [29]. Typical capillary discharge currents used for simulation in ETFLOW code, are shown in Fig. 2, peaking at 50–250 kA ( $\sim 4$  to 20 MA/m<sup>2</sup>) for a capillary of 4 mm diameter.

Investigation of higher ionization states, up to the third ionization, required a modification in the ETFLOW code by adding a routine to obtain the number density of the plasma species and the plasma composition, which is determined from solution of Saha equation, the ionization potentials and the effective average charge state. The added routine calculates the electron ( $n_e$ ), ions ( $n^+$ ,  $n^{++}$  and  $n^{+++}$ ), neutral ( $n_o$ ) and total number density ( $n_{Tot}$ ), which provides an insight on the plasma behavior and the higher ionizations especially for high current discharge (50–250 kA). A modified Saha–Boltzmann equation with relation between the effective charge state  $Z_{eff}$  and the ionization potential  $I_z(Z_{eff} + \frac{1}{2}) = kT \ln(AT^{3/2}/Z_{eff} n)$  is used,

where  $A$  is a constant ( $4.834 \times 10^{21} \text{ K}^{-3/2} \text{ m}^{-3}$ ),  $k$  is Boltzmann's constant,  $n$  is the number density of plasma particles, and  $T$  is the plasma temperature. For quasi-neutrality  $n_e = \sum_{i=1}^{i_{max}} in_i$  and  $Z_{eff} = (an_1 + bn_2 + cn_3)/n_e$ . The number densities  $n_1$ ,  $n_2$  and  $n_3$  weighed with respect to the ionization energy for each state by the corresponding factors  $a$ ,  $b$  and  $c$  represent the ions in the first, second and third ionization, respectively. Number density of ionized species in Saha equation ( $n_e n_{i+1}/n_i$ ) is proportional to  $(g_{i+1}/g_i)e^{-(E_i - \Delta E_i)/kT}$ , where  $i$  is the charge state of plasma species,  $g_i$  is the degeneracy of the  $i$ th electron excitation level,  $E_i$  is the ionization potential of the  $i$ th charge state.  $\Delta E_i = Ze^2/4\pi\epsilon_0\lambda_D$  is a correction term; where  $Z = 1$  is for neutral particles, and  $Z = 2$  is for ionization of singly-charged particles; and  $Z = 3$  or 4 or 5 for higher ionization states. There will be one equation for each ionization state and two for the neutral atom and electron densities, and Saha equation will be solving independently for each of the ionization states.

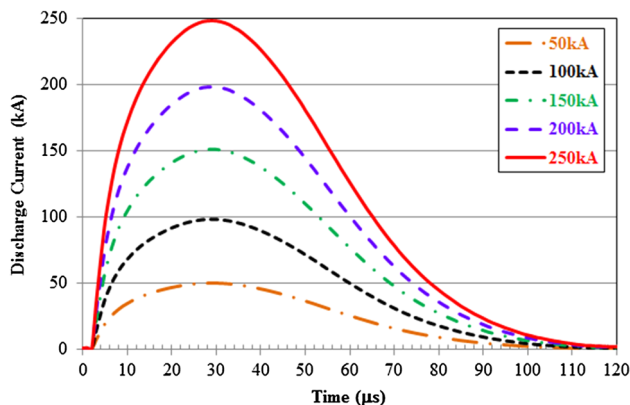


**Fig. 2** Input discharge currents to the electrothermal source (50–150 kA) with  $\sim 50 \mu\text{s}$  effective FWHM

## Results and Discussion

ETFLOW code with new modifications used to conduct an investigation of the generation of higher ionization carbon ions under the nonideality plasma regime. Five simulation runs conducted using carbon as the capillary ablator, with discharge currents of 50, 100, 150, 200 and 250 kA. For each run, the code calculates the spatial and temporal parameters such as the ablated mass and the corresponding heat flux, number density of the individual plasma constituents, plasma temperature and pressure, and plasma bulk velocity. Of interest in this paper are plasma parameters at the capillary exit as this provides information on

the evolution of the plasma into the fusion reactor vacuum vessel. Figure 3 shows the plasma pressure at the capillary exit, indicating a peak pressure of  $3.05 \times 10^8 \text{ N/m}^2$  (305 MPa) at 50 kA to  $2.14 \times 10^9 \text{ N/m}^2$  (2140 MPa) at 250 kA. The pressure peaks at about 15  $\mu\text{s}$  after the peak of the discharge current as the discharge current is the source of Joule heating of the capillary arc, which emits radiant heat flux and initiates surface ablation and ejection of the particulates from the liner material, followed by dissociation and ionization, and hence the pressure buildup follows. Figure 4 shows the peak exit pressure as a function of the peak discharge current, which indicates the increase in the pressure with the increase in the current. While it may appear as a linear trend, however, previous studies have shown power law scaling for most plasma parameters in capillary discharges [27–29]. In this set of results for the nonideal plasma regime, the fitting scaling law  $P_{\text{exit peak}} (\text{N/m}^2) = 3 \times 10^6 I_{\text{peak}}^{1.2027} (\text{kA})$  is in good correlation with published scaling laws [28]. The exit pressure is of importance for the application of electrothermal sources as fusion pellet injectors when the source has an extension barrel to propel the pellet to high velocities necessary for deep fueling of fusion reactor [24].

Time evolution of the plasma temperature at the capillary exit is illustrated in Fig. 5 for the tested range of peak discharge current 50–250 kA. Figure 6 shows Plasma temperature peaks with the peak of the discharge current due to immediate Joule heating and plasma formation ( $E_{\text{Joule}} = J^2/\sigma_{\text{nonideal}}$ ). The plasma temperature for all currents starts at about 5000 K (0.44 eV), and peaks to  $\sim 31,700 \text{ K}$  (2.73 eV) for 50 kA and reaches 47,500 K (4.1 eV) for 250 kA. Close to the end of the discharge

period, all temperatures converge to lower values 12,530 K (1.08 eV) for 50 kA to 19,980 K (1.72 eV) for 250 kA. The scaling of the peak exit temperature with the peak of the discharge current also follows a power law ( $T_{\text{exit peak}} (\text{K}) = 11,914 I_{\text{peak}}^{0.2501} (\text{kA})$ ), which is consistent with published scaling laws for electrothermal plasma sources [27, 28].

Of importance is the high heat flux produced by the capillary, which classifies electrothermal plasma sources as excellent radiant high-heat flux sources for various applications such as evaluation of materials response to transient heat fluxes, simulation of pulsed heat flux impact resulting from a tokamak disruption event, transient heat source for ignition of electrothermal-chemical (ETC) launchers, and pulsed mini-thrusters [30–32]. Figure 7 shows the time evolution of the radiant heat flux at the capillary exit for the range of discharge current between 50 to 250 kA. Radiant heat flux from the plasma core  $q''_{\text{plasma core}}$  peaks with the peak of the temperature ( $q''_{\text{plasma core}} = \sigma_{\text{SB}} T^4$ ), where  $\sigma_{\text{SB}}$  is the Stefan–Boltzmann’s constant for blackbody radiation. However, the heat flux reaching the surface is less due to the vapor shield effect, and hence the heat flux at the wall is ( $q''_{\text{at wall}} = f q''_{\text{plasma core}} = f \sigma_{\text{SB}} T^4$ ), where  $f$  is the vapor shield factor that provides the ratio of the actual heat flux reaching the ablating surface [33]. ETFLOW has two models for vapor shield, one is an opacity model and the second is a ratio model [33]. The code runs with the choice of either model 1 or model 2 or with vapor shield at fixed value (10 or 20%) or with vapor shield turned off. The equation for the  $f$  factor in the code for the ration model is

**Fig. 3** Time evolution of the plasma pressure at the capillary exit for discharge currents between 50 and 250 kA

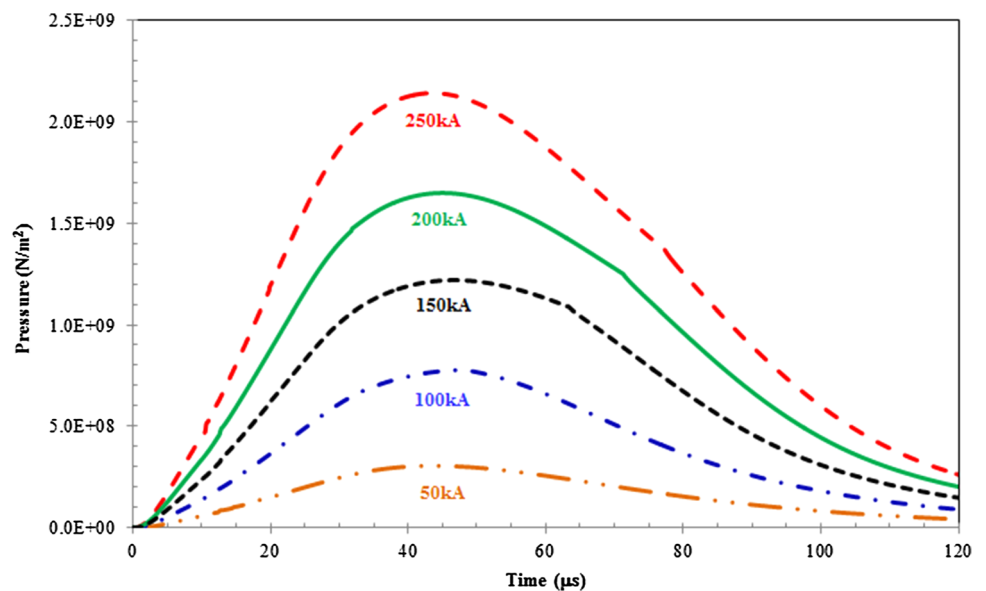


**Fig. 4** Peak exit pressure versus peak discharge current

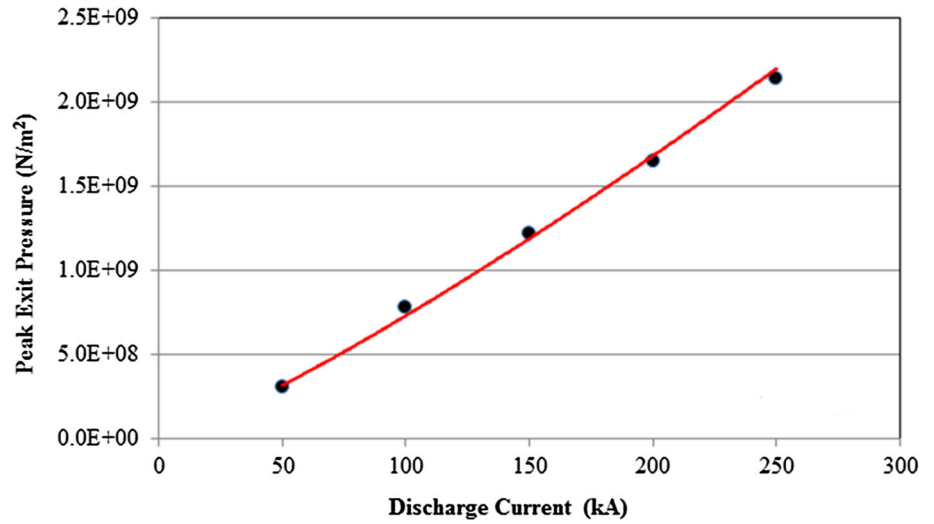


**Fig. 5** Time evolution of the plasma temperature at the capillary exit for discharge currents between 50 and 250 kA

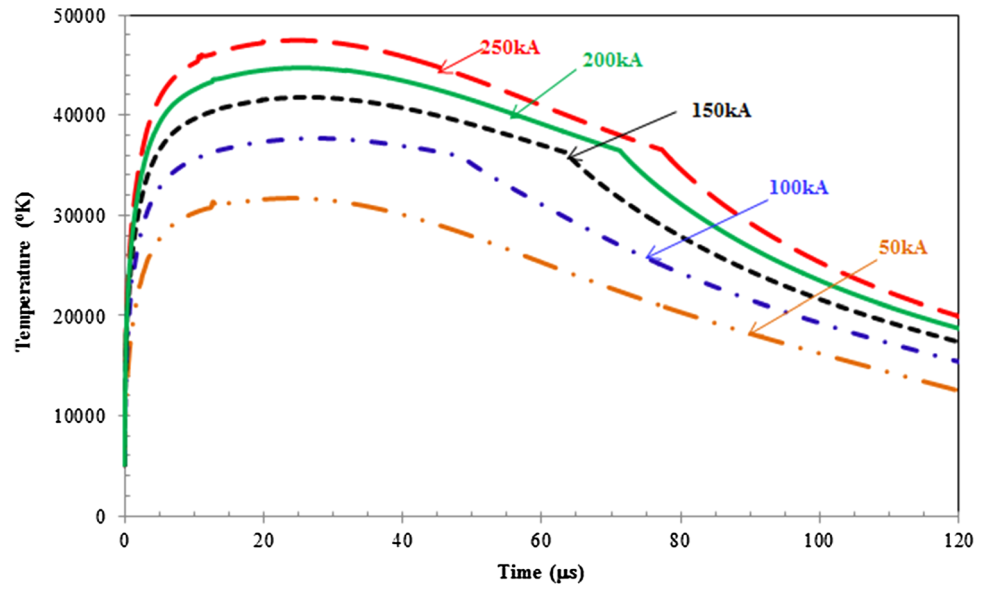


**Fig. 6** Peak exit temperature versus peak discharge current

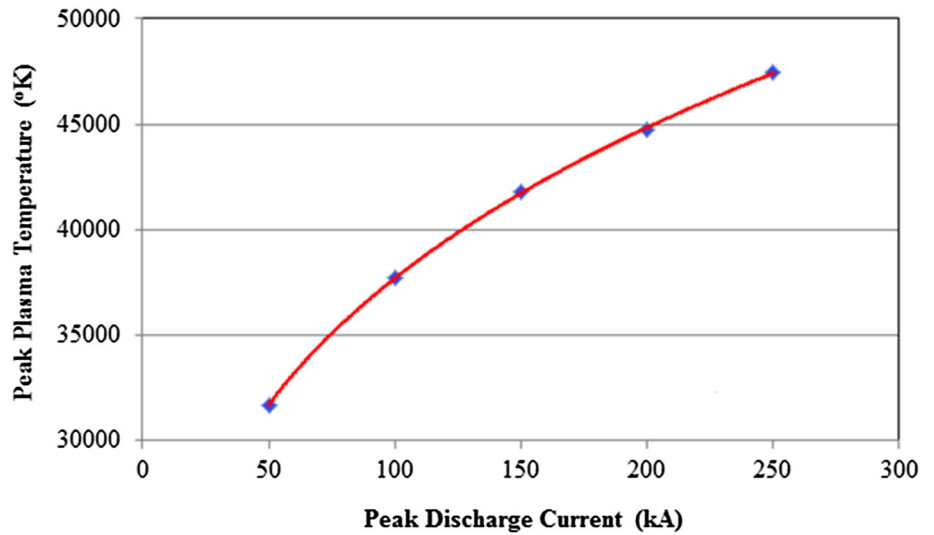
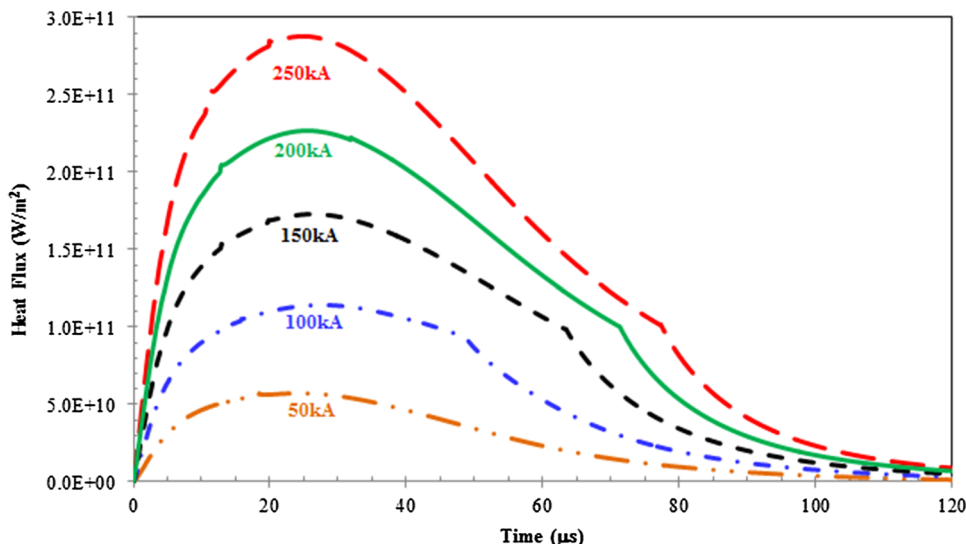


**Fig. 7** Time evolution of the radiant heat flux at the capillary exit for discharge currents between 50 and 250 kA



written as  $f = (\rho H/P + \rho U + \rho H)$ , where  $P$  is the plasma kinetic pressure,  $\rho$  is the plasma density,  $H$  is the sublimation energy and  $U$  is the plasma internal energy. The vapor shield in this model provides 10–20% effect on the ablated mass, and the value of the  $f$  factor varies in time with the rise and fall of the discharge current.

The peak heat flux varies from 57 to 288 GW/m<sup>2</sup> for discharge currents of 50–250 kA, respectively.

The heat flux drops to a minimum for all discharge currents at the end of the discharge time, as shown in Fig. 7, with values between 6.2 and 7.2 GW/m<sup>2</sup> for 50–250 kA, respectively. Figure 8 shows the increase in the peak heat flux with the increase of the discharge current. The scaling of radiant heat flux with discharge current may be taken linearly or in a power law, the data fit a power law ( $q''_{rad\ peak} (W/m^2) = 10^9 I_{peak}^{1.0009} (kA)$ ), which is preferable as all

other plasma parameters are following a power law, and is consistent with published scaling laws [27, 28].

The consequence of ablation due to the incident radiant heat flux on the inner wall of the carbon liner is an increase in the total mass removal with the increase in the heat flux, which relates the amount of ablation  $n_{ab(t)}$  to the radiant heat flux  $q''_{rad}$  and the material’s heat of sublimation,  $n_{ab(t)} \propto (q''_{rad}/H_{sublim})$ , as previously indicated. Figure 9 shows the total ablated mass released from the capillary for current values between 50 and 250 kA. Total ablation for 50 kA is 61.4 mg and increases to 344.3 mg for 250 kA. An increase in the peak current by a factor of 5.0 results in a factor of 5.6 higher total ablated mass.

A fit in a power law is preferable ( $m_{total\ ablated} (mg) = 0.9346 I_{peak}^{1.0738} (kA)$ ) and correlates well to the general scaling of plasma parameters [28]. Mass ablation inside the source

**Fig. 8** Peak radiant heat flux at the capillary exit versus peak discharge current

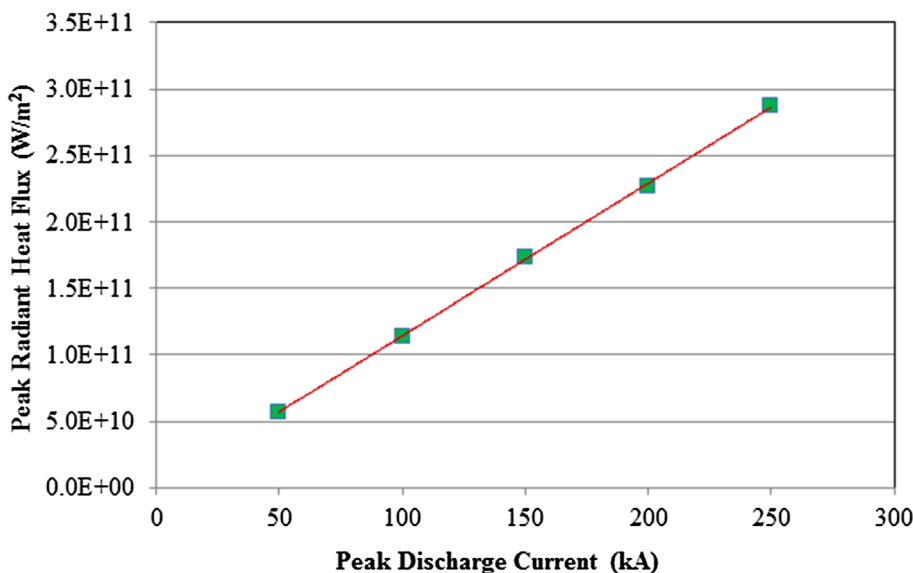
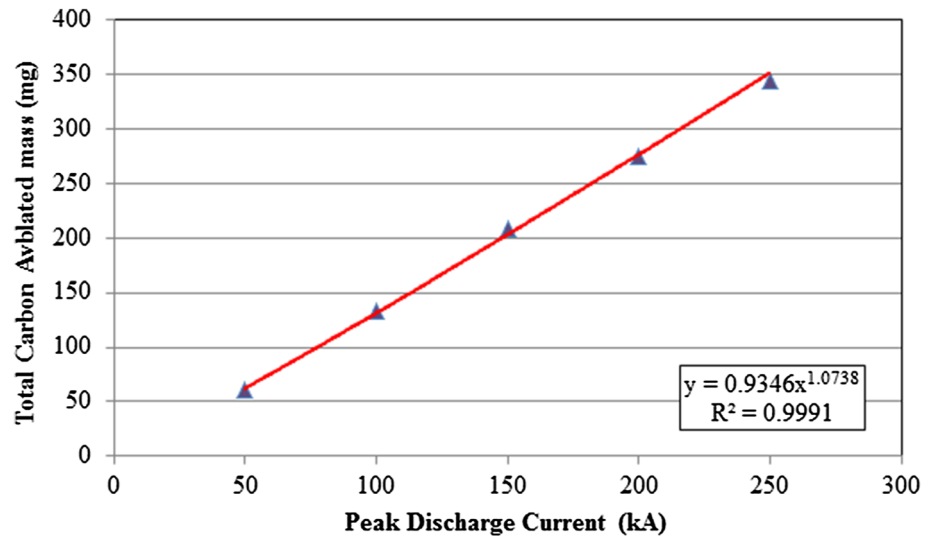




**Fig. 9** Total ablated mass of carbon from the capillary versus peak discharge current



does not include any re-deposition or re-solidification and the total ablated mass removed out of the capillary by the axial flow and the pressure effect.

The total mass ablation leads to the analysis of the plasma composition and the generation of the ionic species, especially the higher ionization states. The interest of this research is to determine the generation of  $C^{++}$  and  $C^{+++}$  ions resulting from high heat flux deposition on carbon (graphite) tiles in tokamak fusion reactors. High-heat flux deposition results in surface evaporation followed by dissociation and ionization, and hence forming partially ionized plasma, which is typical for carbon and CFC tiles in fusion devices [34].

Figure 10 shows the ratio of the neutrals, ionized, and the sum of electron and ionic number densities with respect to the total plasma number density. As seen from the figure, the neutral number density is almost negligible during the first 40  $\mu s$  indicating higher ionization as the discharge current peaks and increases to almost 60% of the total number density at 120  $\mu s$  due to plasma cooling and recombination by the end of the discharge cycle. The sum of electrons and all ions (total quasi-neutral number density  $n_e + \sum n_{ions}$ ) is close to the total number density in the beginning of the discharge and through the first 80  $\mu s$  until recombination takes place near the end of the discharge. Total ionic number density stays almost constant until 80  $\mu s$  and drops to a minimum when the discharge extinguish.

Detailed analysis of the number density of the plasma constituents can be seen in Fig. 11 showing the time evolution of all carbon plasma constituents, electron, ion (first, second and third ionizations), neutrals and the total number density. The ionic number density for first ionization  $C^+$  (peak  $7.52E+26/m^3$ ) closely follows the electron (peak  $1.588E+27/m^3$ ) and total number density (peak  $2.75E+27/$

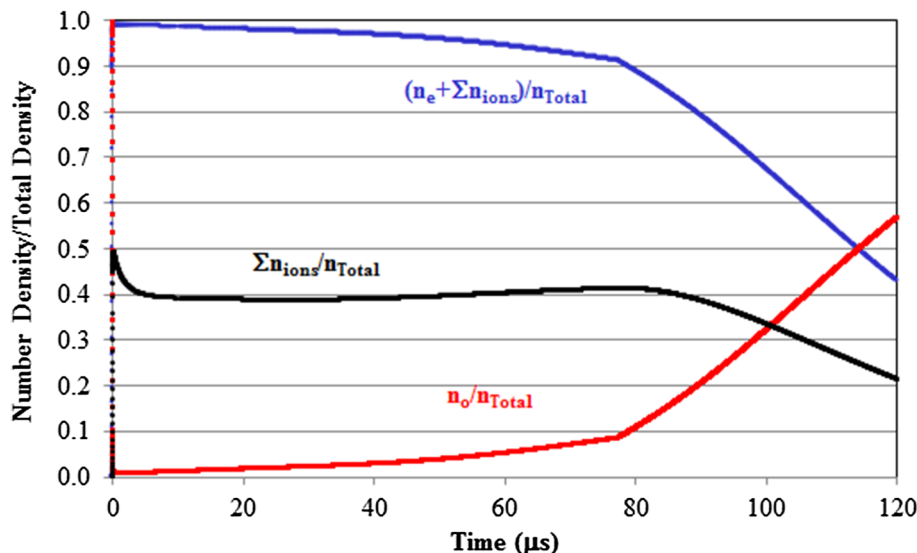
$m^3$ ) over the entire discharge period. The second carbon ionization  $C^{++}$  (peak  $5.09E+26/m^3$ ) is almost equal to the  $C^+$  for the first 45  $\mu s$  then drops at a faster rate towards the end of the discharge cycle due to plasma cooling and recombination. The third ionization  $C^{+++}$  peaks to  $5.51E+24/m^3$  at 35  $\mu s$ , slightly after the peak of the discharge current, then drops at faster rate within less than 60  $\mu s$  to totally disappear at 95  $\mu s$  indicating recombination and capturing electrons thus leaving only first and second ionizations through the end of the discharge.

Figure 12 displays the peak value of the densities versus the peak discharge current for the range 50–250 kA. As seen from the figure the generation of the carbon third ionization is at much a lower rate than that of the second and the first ionizations. However, the number density of the third ionization increases at a higher rate with the increase in the peak discharge current. Scaling of the peak number densities can be determined from the peak discharge current as shown in Eq. 1 set; which also shows the electron and ionic number densities follow a power law for each.

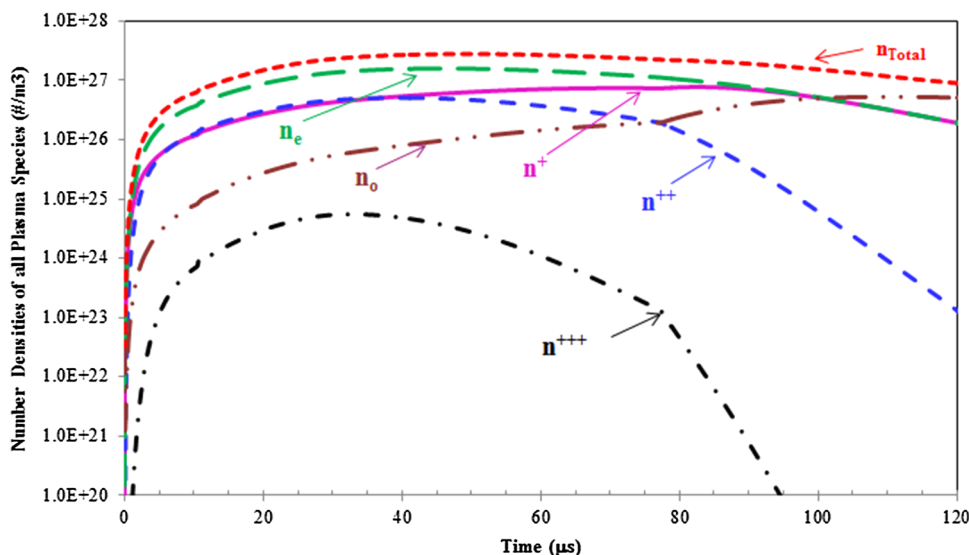
$$\left. \begin{aligned} n_{e(peak)} &= 5 \times 10^{24} I_{peak}^{1.05} \quad (R^2 = 0.9964) \\ n_{i(peak)}^+ &= 2 \times 10^{25} I_{peak}^{0.65} \quad (R^2 = 0.9658) \\ n_{i(peak)}^{++} &= 6 \times 10^{21} I_{peak}^{2.07} \quad (R^2 = 0.9846) \\ n_{i(peak)}^{+++} &= 4 \times 10^{11} I_{peak}^{5.54} \quad (R^2 = 0.9927) \\ n_{o(peak)} &= 5 \times 10^{25} I_{peak}^{0.43} \quad (R^2 = 0.9912) \\ n_{Total(peak)} &= 2 \times 10^{25} I_{peak}^{0.87} \quad (R^2 = 0.9959) \end{aligned} \right\} \quad (1)$$

The plasma bulk velocity at the capillary exit peaks to 5077 m/s for 50 kA peak discharge current and reaches 6507 m/s for 250 kA peak discharge current. Figure 13 shows the time evolution of the plasma bulk velocity at the last node (the capillary exit) for the 50 and 250 kA

**Fig. 10** Time evolution of number densities with respect to the total plasma number density for 250 kA discharge current



**Fig. 11** Time evolution of the number density of the plasma at the capillary exit for 250 kA discharge currents



discharge currents. At the initiation of the plasma formation, the velocity rises sharply to reach its peak at the peak of the discharge current. The higher current has faster rise as compared to lower current values as shown in the figure. The velocity decreases with the decrease in the magnitude of the discharge current and drops from its peak of 5077 m/s for 50 kA to 2964 m/s at the end of the discharge at 120 μs. For higher discharge current of 250 kA, the bulk velocity drops from its peak value of 6507–3811 m/s at 120 μs. It concludes that the exit velocity at the end of the discharge cycle is in the range of 2900–3800 m/s for currents between 50 and 250 kA.

Figure 14 shows a plot between the peak plasma-bulk velocities at the capillary exit versus the peak discharge current. The scaling follows a power law, as all other parameters, and follows  $v_{peak\ at\ exit}^{bulk} (m/s) = 2784.8 I_{peak}^{0.1537} (kA)$  ( $R^2 = 0.9999$ ). All peak velocity values are at 30 μs at the peak of the discharge current. The scaling law correlates to the one previously proposed by Vergara et al. [28], which has the formula  $v = a L^b r^c I_{max}^d \propto I_{max}^d$ , where  $a$ ,  $b$  and  $c$  are coefficients; and  $d$  is the exponent of the power law. The capillary length ( $L$ ) and its radius ( $r$ ) are in meters and the discharge current ( $I_{max}$ ) is the peak value in kA.



**Fig. 12** Peak particle density versus peak discharge current

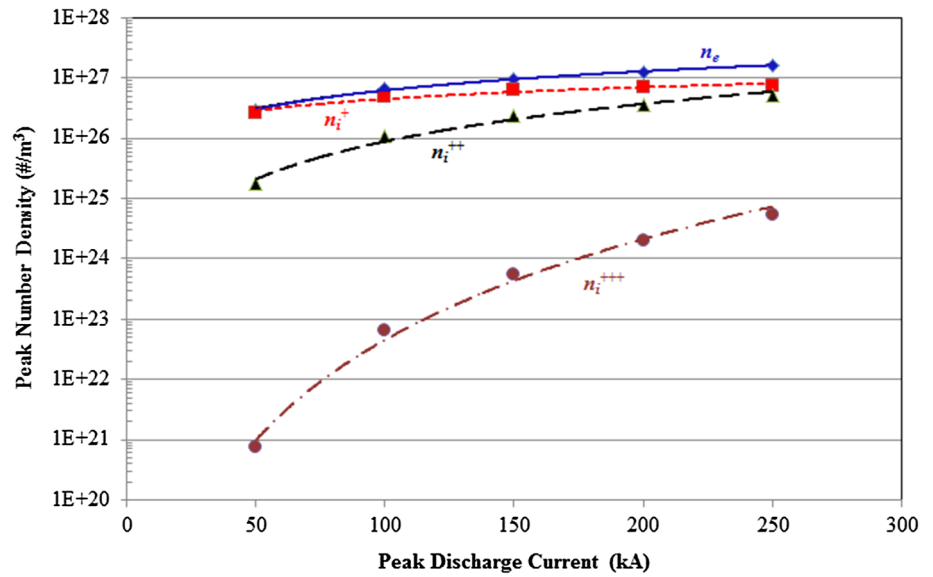
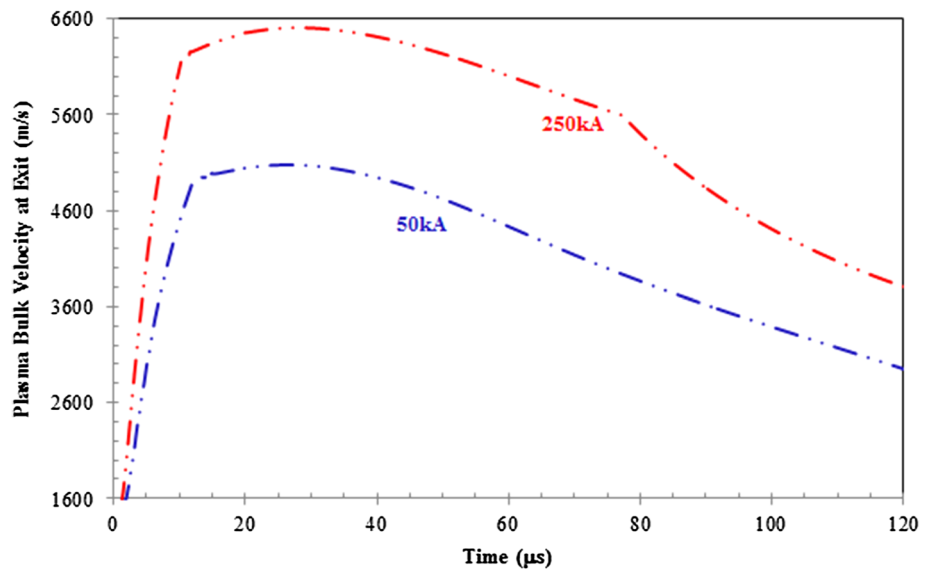


**Fig. 13** Time evolution of the plasma bulk velocity at the capillary exit for 50 and 250 kA discharge currents



**Generalized Scaling Laws for Carbon Capillary Discharge**

The generalized scaling for the peak plasma parameters at the capillary exit can be determined from the peak discharge current as previously shown. The set of scaling in Eq. 1 for the number densities relates to both the peak discharge current and the total mass ablation, as these two parameters are well-measured values. As the total measured ablated mass verified by the scaling law then using the mass and the current together in a set of scaling for the number density will be a useful tool to determine the higher ionizations number densities, as shown in the Eq. 2 set of scaling laws.

$$\left. \begin{aligned}
 n_{e(peak)} &= 5.35 \times 10^{24} I_{peak}^{-0.0238} m_{ablated} \\
 n_{i+(peak)}^+ &= 2.14 \times 10^{25} I_{peak}^{-0.424} m_{ablated} \\
 n_{i+(peak)}^{++} &= 6.42 \times 10^{21} I_{peak}^{0.9962} m_{ablated} \\
 n_{i+(peak)}^{+++} &= 4.28 \times 10^{11} I_{peak}^{4.4662} m_{ablated} \\
 n_{o(peak)} &= 5.35 \times 10^{25} I_{peak}^{-0.6438} m_{ablated} \\
 n_{Total_{peak}} &= 2.14 \times 10^{25} I_{peak}^{-0.2038} m_{ablated}
 \end{aligned} \right\} \quad (2)$$

where the number density is in #/m<sup>3</sup>, peak current is in kA and ablated mass is in mg.

Table 1 shows experimental measurement from two electrothermal plasma sources PIPE and SIRENS [9, 10, 12, 22] where some parameters were successfully

**Fig. 14** Peak plasma bulk velocity at capillary exit versus peak discharge current

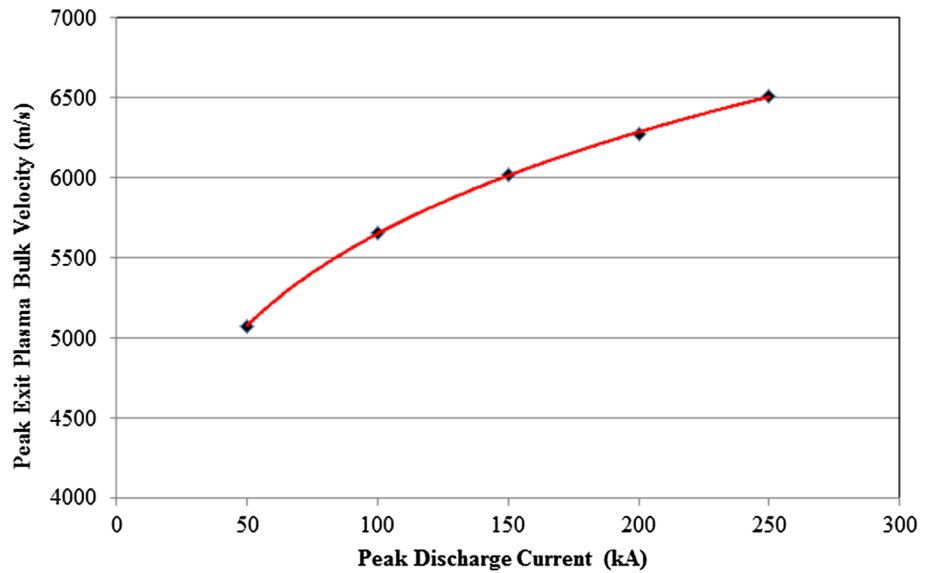


**Table 1** Experimental and predicted parameters from two electrothermal plasma sources

Shot	I <sub>Peak</sub> (kA)	m <sub>Ablated</sub> measured (mg)	m <sub>Ablated</sub> predicted (mg)	P <sub>Exit</sub> measured (MPa)	P <sub>Exit</sub> predicted (MPa)	Predicted density (/m <sup>3</sup> )			
						n <sub>i</sub> <sup>+</sup> × 10 <sup>26</sup>	n <sub>i</sub> <sup>++</sup> × 10 <sup>25</sup>	n <sub>i</sub> <sup>+++</sup> × 10 <sup>20</sup>	N <sub>Total</sub> × 10 <sup>26</sup>
P197	29.61	<b>34.27 ± 6.85</b>	<b>35.54</b>	N/A	159.69	1.892	0.667	0.5673	3.8123
P228	38.98	<b>48.18 ± 9.64</b>	<b>47.74</b>	N/A	228.39	2.162	1.180	2.602	4.8425
P206	42.81	<b>46.87 ± 9.37</b>	<b>52.79</b>	N/A	275.03	2.297	1.430	4.374	5.2539
S783	41.10	<b>53.07 ± 10.61</b>	<b>50.93</b>	<b>249.31</b>	<b>256.07</b>	2.231	1.320	3.607	5.1030
S792	42.48	<b>53.85 ± 10.77</b>	<b>52.38</b>	<b>280.47</b>	<b>272.91</b>	2.279	1.419	4.340	5.2539
S788	65.52	<b>71.73 ± 14.35</b>	<b>82.67</b>	<b>498.61</b>	<b>454.48</b>	3.014	3.395	44.219	7.5556

**Table 2** Predicted carbon ions number density with respect to the total plasma number density

I <sub>peak</sub> (kA)	n <sub>Total</sub> (/m <sup>3</sup> )	% N <sup>+</sup> /n <sub>Total</sub>	% N <sup>++</sup> /n <sub>Total</sub>	% N <sup>+++</sup> /n <sub>Total</sub>
29.61	3.81E+26	47.42	1.75	1.49E−05
38.98	4.84E+26	44.64	2.43	5.37E−05
41.10	5.10E+26	44.05	2.62	7.07E−05
41.40	5.10E+26	44.05	2.62	7.12E−05
42.81	5.25E+26	43.73	2.72	8.33E−05
42.48	5.25E+26	43.73	2.72	8.26E−05
65.52	7.56E+26	39.88	4.49	5.85E−04
70.56	8.11E+26	39.17	4.96	8.59E−04
77.76	8.83E+26	38.34	5.57	1.35E−03
<b>100</b>	1.09E+27	36.27	7.54	4.38E−03
<b>150</b>	1.56E+27	33.18	12.26	2.90E−02
<b>200</b>	2.01E+27	31.14	17.31	1.10E−01
<b>250</b>	2.44E+27	29.65	22.63	3.10E−01

measured. The table shows these experimental results and the corresponding predicted values from the ETFLOW code. The ion number densities are all predicted values. The table shows good correlation between measured and

predicted values of ablated mass and the exit pressure, which correlates well to the scaling laws and provides reasonable confidence in the predicted number density of the plasma species. Data from experimental shots P197,

206, 208 and 228 are from the PIPE experiment and shots S783, 788, 790, 792 and 809 are taken from the SIRENS experiment. Predicted ablated masses and exit pressures are in good agreement with measured ones as shown in Table 1 (bolded data).

Table 2 illustrates the percent of predicted carbon ions number density (first, second and third ionization) with respect to the total plasma number density. The number density of the first ionization is between 47.42 and 29.65% of the total number density indicating a decrease in the first ionization with the increase in the magnitude of the discharge current. Obviously, the second ionization percentage increases from 1.75 to 22.63% with increased peak of the discharge current, and similarly for the third ionization percentage increases from  $1.49 \times 10^{-5}$  to  $3.1E-01$ . While the fraction of the third ionization is very small, however, it is evidential that there will be a fraction of higher ionization carbon ions in the plasma stream. The first data set for discharge currents between 29.61 and 77.76 kA are calculated for the experiments conducted on the ET facilities PIPE and SIRENS. All values between 100 and 250 kA (bolded data) are computationally calculated for the purpose of predictions for higher heat fluxes.

## Conclusions

Generated carbon ions from ablation mechanism in electrothermal plasma sources was calculated using the ETFLOW code as a high-heat flux source simulating disruption-like condition in fusion tokamak reactors. Simulation was conducted using peak discharge currents of 50–250 kA, which produces heat fluxes from 57 to 288 GW/m<sup>2</sup> to explore generation of carbon plasma up to the third ionization C<sup>+++</sup>. The third ionization is six orders of magnitude less than the first ionization at the lowest heat flux and two orders of magnitude less at the highest heat flux. Plasma temperature varies from 31,600 K (2.722 eV) to 47,500 K (4.092 eV) at the lowest and highest heat fluxes, respectively. The plasma temperature and number density indicate typical high-density weakly nonideal plasma.

A set of scaling equations in power law obtained for the plasma parameters at the source exit based on the peak discharge current. The scaling of the ablated mass, as a measurable quantity, was used to relate the number densities to both peak discharge current and total ablated mass, both are measurable parameters, to develop scaling laws for the electron, ion (first, second and third ionization), neutral and total number densities. Some measured parameters, ablated mass and peak exit pressure, obtained from two experiments used to verify the scaling laws and is showing good correlation between measured and predicted

results. The developed scaling used to predict the percentage of each ionic species to the total number density, where the number density of the first ionization is the highest percentage followed by the second then the third, as expected. While the fraction of the third ionization is very small, however, it is evidential that there will be a fraction of higher ionization carbon ions (C<sup>+++</sup>) in the plasma stream.

## References

1. A. Hassanein, Disruption damage to plasma-facing components from various plasma instabilities. *Fusion Technol.* **30**(3), 713–719 (1996)
2. J. Arnoux et al., Heat loads on plasma facing components during disruptions on JET. *Nucl. Fusion* **49**, 085038 (2009)
3. R.A. Pitts et al., Physics basis and design of the ITER plasma-facing components. *J. Nucl. Mater.* **415**(1), S957–S964 (2011)
4. A. Miyahara, T. Tanabe, Graphite as plasma-facing material. *J. Nucl. Mater.* **155–157**(Part 1), 49–57 (1988)
5. R.D. Penzhorn et al., Tritium depth profiles in graphite and carbon fibre composite material exposed to tokamak plasmas. *J. Nucl. Mater.* **288**(2–3), 170–178 (2001)
6. D.G. Whyte et al., The effect of detachment on carbon divertor erosion/redeposition in the DIII-D tokamak. *Nucl. Fusion* **41**(9), 1243–1252 (2001)
7. J.L. Luxon, A design retrospective of the DIII-D tokamak. *Nucl. Fusion* **42**, 614–633 (2002)
8. O.I. Buzhinskij et al., Modification of the graphite tiles surface in tokamaks. *Plasma Devices Oper.* **13**(3), 193–198 (2006)
9. J. Gilligan, M. Bourham, The use of an electrothermal plasma gun to simulate the extremely high heat flux conditions of a tokamak disruption. *J. Fusion Energ.* **12**, 311–316 (1993)
10. G.E. Dale, M.A. Bourham, Experimental investigation into melt layer erosion of plasma-facing materials. *Fusion Technol.* **34**, 901–907 (1998)
11. Nouf Almousa, John Gilligan, Mohamed Bourham, Surface ablation and melting of fusion materials simulated by transient high heat flux generated in an electrothermal plasma source. *IEEE Trans. Plasma Sci.* **44**(9), 1642–1648 (2016)
12. J.P. Sharpe, M.A. Bourham, J.G. Gilligan, Experimental investigation of disruption-induced aerosol mobilization in accident scenarios of ITER, in *Proceedings of 17th IEEE NPSS Symposium on Fusion Engineering*, San Diego, CA, 6–10 Oct 1997, vol. 1, pp. 153–156, 1997
13. J.M. Linke, T. Hirai, M. Rödiger, L.A. Singheiser, Performance of plasma-facing materials under intense thermal loads in tokamaks and stellarators. *Fusion Sci. Technol.* **46**, 142–151 (2004)
14. A. Hassanein, I. Konkashbaev, Comprehensive model for disruption erosion in a reactor environment. *J. Nucl. Mater.* **220–222**, 244–248 (1995)
15. J.R. Echols, A.L. Winfrey, Ablation of fusion materials exposed to high heat flux in an electrothermal plasma discharge as a simulation for hard disruption. *J. Fusion Energ.* **33**, 60–67 (2014)
16. N. Sauthoff et al., Physics requirements for ITER engineering systems, in *Proceedings of 16th IEEE NPSS Symposium Fusion Engineering*, Urbana Champaign, IL, Sept. 30–Oct. 5, vol. 1, pp. 130–137, 1995
17. V. Barabash, G. Federici, R. Matera, A.R. Raffray, ITER Home Teams, Armour materials for the ITER plasma facing components. *Phys. Scr.* **T81**, 74–83 (1999)

18. M. Rubel et al., Beryllium and carbon films in JET following D-T operation. *J. Nucl. Mater.* **313–316**, 321–326 (2003)
19. M. Seki, S. Yamazaki, A. Minato, T. Horie, Y. Tanaka, T. Tone, A simulated plasma disruption experiment using an electron beam as a heat source. *J. Fusion Energ.* **5**(3), 181–189 (1986)
20. P.D. Rockett et al., Studies of the ablated plasma from experimental plasma gun disruption simulations. *J. Nucl. Mater.* **220–222**, 785–789 (1995)
21. A. Kirschnera, V. Philippsa, J. Winterb, U. Köglera, Simulation of the plasma–wall interaction in a tokamak with the Monte Carlo code ERO-TEXTOR. *Nucl. Fusion* **40**(5), 989–1001 (2000)
22. J.P. Sharpe, B.J. Merrill, D.A. Petti, M.A. Bourham, J.G. Gilligan, Modeling of particulate production in the SIRENS plasma disruption simulator. *J. Nucl. Mater.* **290**, 1128–1133 (2001)
23. E. Vietzke, A. Refke, V. Philipps, M. Hennes, Energy distributions of the reaction products from graphite and B<sub>4</sub>C during energetic oxygen impact. *J. Nucl. Mater.* **220–222**, 249–253 (1995)
24. T.E. Gebhart, R.T. Holladay, M.J. Esmond, A.L. Winfrey, The effect of pellet volume and aspect ratio on fuel pellet exit velocities in a capillary discharge mass accelerator, in *Proceedings of 2013 IEEE 25th Symposium on Fusion Energy (SOFE)*, Francisco, CA, 10–14 June 2013, pp. 1–6. doi:10.1109/SOFE.2013.6635502
25. M.R. Zaghloul, M. Al-Naiemy, M.A. Bourham, Measurement of electrical conductivity of weakly non-ideal multi-component plasma mixtures generated from dielectric materials. *IEEE Trans. Plasma Sci.* **37**(8), 1626–1631 (2009)
26. L. Winfrey, J. Gilligan, A. Saveliev, M. Abd Al-Halim, M. Bourham, A study of plasma parameters in a capillary discharge with calculations using ideal and non-ideal plasma models for comparison with experiment. *IEEE Trans. Plasma Sci.* **40**(3), 843–852 (2012)
27. M.A. Abd Al-Halim, M.A. Bourham, Characterization of short intense pulsed electrothermal plasma capillaries for use as fusion and launchers heat flux sources. *J. Fusion Energ.* **33**, 258–263 (2014)
28. P.P. Vergara, J. Gilligan, L. Winfrey, M. Bourham, Generalized scaling laws of plasma parameters in electrothermal plasma sources for fusion disruption erosion and hypervelocity launch applications. *IEEE Trans. Plasma Sci.* **43**(10), 3645–3652 (2015)
29. M.R. Zaghloul, M.A. Bourham, J.M. Doster, J.D. Powell, On the average electron–ion momentum transport cross-section in ideal and non-ideal plasmas. *Phys. Lett. A* **262**, 86–89 (1999)
30. T. Edamitsu, H. Tahara, Experimental and numerical study of an electrothermal pulsed plasma thruster for small satellites. *Vacuum* **80**(11/12), 1223–1228 (2006)
31. L. Pekker, Zero-dimensional time-dependent model of high pressure ablative capillary discharge for plasma thrusters. *J. Propuls. Power* **24**(4), 958–969 (2009)
32. A.J. Porwitzky, M. Keidar, I.D. Boyd, Progress towards an end-to-end model of an electrothermal chemical gun. *IEEE Trans. Magn.* **45**, 412–416 (2009)
33. N. AlMousa, M. Bourham, Vapor shield models for fusion reactors plasma facing components. *J. Fusion Energ.* **35**(5), 786–794 (2016)
34. K. Nakamura et al., High heat flux experiments of plasma facing components for next fusion devices, in *Proceedings of 15th IEEE NPSS Symposium on Fusion Engineering (SOFE)*, Hyannis, MA, 11–15 Oct 1993, vol. 2, pp. 830–833, 1993